

## Article

# Evaluation of the Impact of Morphological Differences on Scale Effects in Green Tide Area Estimation

Ke Wu <sup>1</sup>, Tao Xie <sup>1,2,3,4,\*</sup>, Jian Li <sup>1</sup>, Chao Wang <sup>5</sup>, Xuehong Zhang <sup>1</sup>, Hui Liu <sup>1</sup> and Shuying Bai <sup>1</sup>

<sup>1</sup> School of Remote Sensing and Geomatics Engineering, Nanjing University of Information Science and Technology, Nanjing 210044, China; 202491000002@nuist.edu.cn (K.W.); 003233@nuist.edu.cn (J.L.); zxbnu@nuist.edu.cn (X.Z.); huil@nuist.edu.cn (H.L.); 001462@nuist.edu.cn (S.B.)

<sup>2</sup> Laboratory for Regional Oceanography and Numerical Modeling, Qingdao Marine Science and Technology Center, Qingdao 266237, China

<sup>3</sup> Technology Innovation Center for Integration Applications in Remote Sensing and Navigation, Ministry of Natural Resources, Nanjing 210044, China

<sup>4</sup> Jiangsu Province Engineering Research Center for Collaborative Navigation/Positioning and Smart Application, Nanjing 210044, China

<sup>5</sup> School of Electronics and Information Engineering, Nanjing University of Information Science and Technology, Nanjing 210044, China; chaowang@nuist.edu.cn

\* Correspondence: xietao@nuist.edu.cn

**Abstract:** Green tide area is a crucial indicator for monitoring green tide dynamics. However, scale effects arising from differences in image resolution can lead to estimation errors. Current pixel-level and sub-pixel-level methods often overlook the impact of morphological differences across varying resolutions. To address this, our study examines the influence of morphological diversity on green tide area estimation using GF-1 WFV data and the Virtual-Baseline Floating macroAlgae Height (VB-FAH) index at a 16 m resolution. Green tide patches were categorized into small, medium, and large sizes, and morphological features such as elongation, compactness, convexity, fractal dimension, and morphological complexity were designed and analyzed. Machine learning models, including Extra Trees, LightGBM, and Random Forest, among others, classified medium and large patches into striped and non-striped types, with Extra Trees achieving outstanding performance (accuracy: 0.9844, kappa: 0.9629, F1-score: 0.9844, MIoU: 0.9637). The results highlighted that large patches maintained stable morphological characteristics across resolutions, while small and medium patches were more sensitive to scale, with increased estimation errors at lower resolutions. Striped patches, particularly among medium patches, were more sensitive to scale effects compared to non-striped ones. The study suggests that incorporating morphological features of patches, especially in monitoring striped and small patches, could be a key direction for improving the accuracy of green tide monitoring and dynamic change analysis.

**Keywords:** green tide area; scale effects; morphological feature; fractal dimension; striped patches; resolution sensitivity



Academic Editors: Gabriel Navarro and Teodosio Lacava

Received: 29 November 2024

Revised: 10 January 2025

Accepted: 16 January 2025

Published: 18 January 2025

**Citation:** Wu, K.; Xie, T.; Li, J.;

Wang, C.; Zhang, X.; Liu, H.; Bai, S.

Evaluation of the Impact of

Morphological Differences on Scale

Effects in Green Tide Area Estimation.

*Remote Sens.* **2025**, *17*, 326. [https://](https://doi.org/10.3390/rs17020326)

[doi.org/10.3390/rs17020326](https://doi.org/10.3390/rs17020326)

**Copyright:** © 2025 by the authors.

Licensee MDPI, Basel, Switzerland.

This article is an open access article

distributed under the terms and

conditions of the Creative Commons

Attribution (CC BY) license

([https://creativecommons.org/](https://creativecommons.org/licenses/by/4.0/)

[licenses/by/4.0/](https://creativecommons.org/licenses/by/4.0/)).

## 1. Introduction

The excessive proliferation of *Ulva prolifera* in coastal areas leads to large-scale marine green tides, which harm the ecosystem and economy [1,2]. Satellite remote sensing data support green tide early warning, monitoring, and post-event assessment [3,4]. They also provide technical and data support for green tide prevention, coastal protection, and aquaculture [5,6]. Green tide area is a crucial indicator in green tide detection, making the selection of an appropriate estimation method essential [7,8].

Traditional index-based green tide extraction methods calculate the index value for each pixel and use a threshold to determine the presence of *Ulva prolifera*, thus identifying the spatial distribution of the green tide [9]. Based on spectral response characteristics, researchers have designed and applied methods such as the Normalized Difference Vegetation Index (NDVI) [10], Normalized Difference Algae Index (NDAI) [11], Scaled Algae Index (SAI) [12,13], Floating Algae Index (FAI) [14], and Virtual Baseline Floating macroAlgae Height (VB-FAH) [15] for green tide extraction. While effective to some extent, these traditional methods have limitations when faced with complex environmental conditions and changes in spectral characteristics [16]. Notably, in cases where green tide coverage is sparse, the background is complex, or there is spectral mixing, the accuracy and robustness of these methods may be significantly impacted [17], highlighting the need for innovation and improvement in green tide extraction methods. With the rapid development of artificial intelligence technologies, deep-learning-based remote sensing image processing methods have gradually been applied to green tide extraction and monitoring [18–20]. The application of artificial intelligence in green tide extraction not only provides breakthroughs in methodology but also significantly improves the efficiency and accuracy of green tide monitoring, especially in areas with complex sea backgrounds and severe spectral confusion [21,22]. By leveraging deep learning's automatic feature extraction, image enhancement, and time-series analysis capabilities, researchers have overcome many of the limitations of traditional methods, significantly improving the accuracy and reliability of green tide extraction [23,24].

Traditional and emerging deep-learning-based extraction methods are essentially pixel-level semantic segmentation techniques. However, due to differences in the spatial resolution of satellite payloads used by researchers, estimating green tide areas from different remote sensing data has an inherent scale effects. For example, high-resolution images can capture the boundaries and details of green tide more clearly, while low-resolution images may lead to underestimation or overestimation of green tide areas. To address the scale effects in remote sensing, researchers have proposed methods for calculating the areas of objects at the subpixel level. Standard techniques include the Linear Unmixing Algorithm (LA) [25], Algae Pixel-Growing Algorithm (APA) [26], Spectral Mixture Analysis (SMA) [27–29], and Fractional Pixel (FP) model [30,31]. For instance, APA estimates the coverage area of algal blooms in Lake Taihu at the subpixel level. First, it identifies the “growth point” pixels of algae in the image, and then, by analyzing the spectral and spatial characteristics of adjacent pixels, it gradually extends the algal bloom area to neighboring pixels to obtain a more refined coverage estimate. APA combines FAI and LA to dynamically adjust and optimize the algae coverage ratio within each mixed pixel. SMA analyzes the spectral contribution of different objects within a pixel and decomposes the spectral characteristics of the original pixel into a weighted combination of multiple subpixel components, thus quantifying the coverage degree of each target object. The FP model estimates the coverage area of the target object in low-resolution data by utilizing the target's characteristic spectra and the image's local spatial information.

By performing subpixel-level calculations, researchers can obtain more refined and reliable information on the distribution of green tide and more accurate estimates of green tide coverage. However, this method for mitigating the scale effects is mainly limited to analyzing pixel values or spatial correlations between pixels without fully utilizing the morphological characteristics of green tide patches. The morphological study of green tide focuses on the shape, size, edge characteristics, and connectivity of patches, which not only reflect the growth state and spread pattern of the green tide but also provide richer information for monitoring and estimating green tide areas. As shown in Figure 1, the morphological characteristics of patches are primarily represented by scattered small

patches (Figure 1a,b) and morphologically diverse large patches. Small patches are visible in high-resolution images. However, as the resolution decreases, their detection signal weakens and may even disappear, leading to an underestimation of green tide coverage, which is one of the critical causes of the scale effects. Large patches are typically strip-like, possibly due to the drifting of the green tide with ocean currents and the rapid proliferation of *Ulva prolifera* during drift. Striped patches (Figure 1c,d) are narrow, with a higher proportion of edge pixels, making them more prone to being recognized as mixed pixels in low-resolution images, which weakens their detection signal and exacerbates the scale effects. As the drift speed slows and factors such as ocean currents and wind direction change, striped patches gradually merge to form larger non-striped patches (Figure 1e,f). During this process, due to the movement of patches and the proliferation or decay of *Ulva prolifera*, the morphology of new patches becomes highly complex, differing significantly from striped patches. Although non-striped patches have relatively fewer edge pixels, they are usually large, with many holes and fragmented boundaries. In low-resolution images, pixels around the edges and holes are still recognized as mixed pixels, so the scale effects persists. Therefore, analyzing the morphological characteristics of green tide patches provides significant potential and feasibility for reducing the scale effects in area estimation.

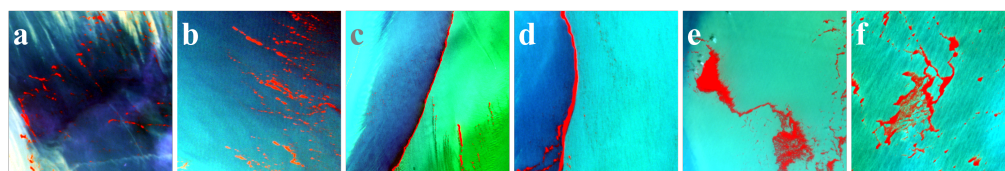


**Figure 1.** False-color composite images of patches with three different morphologies. Subfigures (a,b): small patches; subfigures (c,d): striped patches; subfigures (e,f): non striped patches. The red pixels in the false color image is the green tide pixels.

Due to the imbalance between the satellite image swath width and spatial resolution, multi-source satellite collaborative monitoring of green tide may become an essential technological approach in the future. Researchers have advanced green tide monitoring through different approaches: some have developed fusion modules integrating multi-source satellite data, leveraging resampling, area refinement, and drift tracking to produce consistent, comprehensive products that enhance prediction efficiency [32]. Others have combined optical and SAR remote sensing data to analyze spatiotemporal correlations between marine aquaculture and green tide outbreaks, offering critical insights into balancing marine environmental protection and resource management [33]. Given that the spatial distribution of green tide and the green tide coverage within each pixel must be accurate, the scale effects in collaborative monitoring deserve attention. Therefore, this study aims to evaluate the impact of different patch morphologies on the scale effects. First, a classification was performed based on the morphological features of the patches, where various morphological features were designed and introduced as the basis for classification. The results demonstrated high classification accuracy, confirming the feasibility of classifying patches based on these features. Subsequently, the classification model was applied to conduct a full-range analysis of patch morphologies across the study area. Through this, resampling was employed to simulate patches at different resolutions, allowing an assessment of the area loss for various morphological patch types during the resolution reduction process, and fitting equations for patch area at each resolution were derived. Finally, the results were summarized, focusing on the necessity and feasibility of incorporating patch morphological factors in future green tide collaborative monitoring tasks.

## 2. Materials and Methods

### 2.1. Data Collection and Green Tide Detection

We selected GF-1 satellite WFV (wide field of view) data with a sufficiently high spatial resolution to study green tide patch morphology. Interference factors such as clouds and glare were manually removed, leaving areas that predominantly contain green tide and seawater. Since most interference factors had been manually eliminated, traditional index-based methods were chosen for green tide detection. The study area is located in the Yellow Sea of China, where green tide events have frequently occurred in recent years, with coordinates ranging from 31° to 37°N and 119° to 125°E. The GF-1 images were obtained from the China Resource Satellite Application Center (<https://data.cresda.cn/#/home>, accessed on 20 September 2024). The satellite was developed by the China Academy of Space Technology (CAST), based in Beijing, China. The primary sensor parameters are shown in Table 1. The research data include approximately 85 images from the Yellow Sea between 2015 and 2024. The images were processed through radiometric calibration, atmospheric correction, and geometric correction, resulting in the bottom of atmosphere (BOA) reflectance. The green tide detection index chosen for this study is VB-FAH, with the calculation formula as follows:

$$\text{VB-FAH} = (R_4 - R_2) + \frac{(R_2 - R_3) \cdot (\lambda_4 - \lambda_2)}{2\lambda_4 - \lambda_3 - \lambda_2} \quad (1)$$

where  $R_4$ ,  $R_3$ , and  $R_2$  represent the BOA reflectance in the near-infrared, red, and green bands, respectively;  $\lambda_4$ ,  $\lambda_3$ , and  $\lambda_2$  represent the central wavelengths of the near-infrared, red, and green bands, respectively. The VB-FAH threshold fluctuates within the range of 0.015 to 0.035, with the exact value selected based on the specific conditions of the image. Pixels with a value above this threshold are detected as green tide pixels.

**Table 1.** Main parameters of the GF-1 WFV sensor.

Band	Bandwidth (nm)	Spatial Resolution (m)	Central Wavelength (nm)
Blue	450–520	16	485
Green	520–590	16	555
Red	630–690	16	645
NIR	770–890	16	830

### 2.2. Patch Segmentation

After obtaining the green tide extraction results using the VB-FAH index, the Connected Component Labeling (CCL) algorithm was applied to segment and extract all the patches [34]. The basic idea of this algorithm is to label all connected target pixels through two scans of the image, where connected pixels are groups of pixels with the same attributes [35]. The connectivity used is 8-connectivity, meaning that a pixel is connected to its neighboring pixels in the vertical, horizontal, and diagonal directions.

First, assume the image is represented by a binary matrix  $I$ , where the target pixels have a value of 1, and the background pixels have a value of 0. The first step of the CCL algorithm is to scan matrix  $I$  and label all connected target pixels with the same connectivity label using an equivalence table. During this process, for the current pixel  $I(i, j)$ , the following rules are applied based on its labeled neighboring pixels:

1. If  $I(i, j)$  is a target pixel and at least one neighboring pixel is already labeled, the current pixel is labeled with the same label as the neighboring pixel.
2. If multiple neighboring pixels have different labels, their equivalence relationship is recorded in the equivalence table, and the current pixel is assigned the smaller label.

3. A new label is assigned to the current pixel if no neighboring pixels are labeled.

After the first scan, initial labels for all target pixels are obtained, and an equivalence table is created. During the second scan, the labels are updated according to the equivalence table, ensuring that all connected components with equivalent labels have the same label. Finally, each label represents an independent patch. Through this process, segmentation and extraction results for all patches are obtained, resulting in approximately 1.04 million binary images, where pixels with a value of 1 represent green tide pixels, and those with a value of 0 represent non-green tide pixels.

### 2.3. Patch Classification Based on Size

Regarding patch size, patches that are too small typically do not exhibit significant morphological differences between “striped” and “non-striped” forms, especially in satellite imagery. These small patches often have only a few pixels and lack prominent morphological features. Therefore, the research value of their morphological characteristics is relatively limited. Although some morphological differences can be observed for medium and large patches, the extent of elongation in striped patches or the complexity in non-striped patches can vary significantly due to differences in size. Therefore, it is necessary to conduct distinct morphological studies for patches of different sizes to more comprehensively assess their morphological characteristics and the impact of size on scale effects.

In this study, the size of a patch is defined as the maximum value between the length and width of the patch image. By analyzing the distribution of patch sizes, the point with the most significant gradient change in the data distribution was selected as the threshold for size classification, which was determined to be 26.67 pixels and 99.10 pixels. Accordingly, patches between [1, 26] pixels are classified as small patches, patches between [27, 99] pixels as medium patches, and patches larger than 99 pixels as large patches. The quantity and area proportions of the three patch types are shown in Figure 2. It can be observed that small patches account for nearly 80% of the total quantity, far exceeding medium and large patches. However, in terms of area, medium and large patches account for more than 90%, with large patches alone covering 78.5% of the total area. Therefore, medium and large patches play a dominant role in calculating green tide coverage area, but the impact of all three patch types on scale effects requires further investigation.

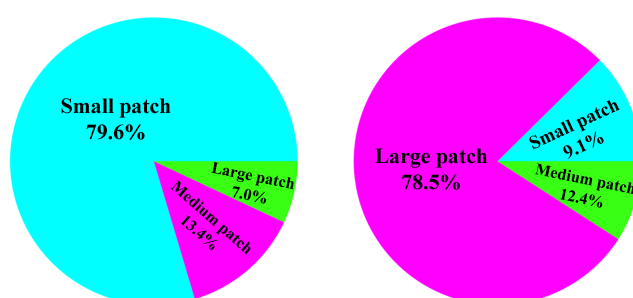


**Figure 2.** Proportions of quantity (a) and area (b) for three patch types.

### 2.4. Elongation, Compactness, Convexity and Concavity

Various morphological features, including elongation, compactness, convexity, concavity, fractal dimension, and morphological complexity, were introduced to explore further the impact of patch morphology on the scale effect. These features provide essential criteria for morphology-based patch classification and contribute to a deeper understanding of green tides’ growth and decay patterns.

Based on patches' fundamental characteristics (such as perimeter, area, and the number of holes), various morphological features were designed to quantify the patch's extensibility, compactness, and convexity/concavity, as shown in Figure 3.

The elongation index  $E$  is defined to quantify the extent of patch elongation. It is calculated as the ratio of the maximum Manhattan distance between any two pixels within the patch to the total number of pixels in the patch (Figure 3a):

$$E = \frac{D_{\max}}{N} \quad (2)$$

where  $D_{\max}$  represents the maximum Manhattan distance between any two pixels within the patch, and is calculated as follows:

$$D_{\max} = \max_{i,j} (|x_i - x_j| + |y_i - y_j|) \quad (3)$$

where  $(x_i, y_i)$  and  $(x_j, y_j)$  represent the coordinates of the  $i$ -th and  $j$ -th pixels within the patch, and  $|\cdot|$  denotes the absolute value operation;  $N$  is the total number of pixels in the patch. The elongation index  $E$  reflects the extent of the patch's elongation. As  $E$  approaches 1, it indicates that a more significant proportion of the pixels along the path of the maximum Manhattan distance are within the patch, suggesting that the patch is more "slender". Conversely, as  $E$  approaches 0, the patch becomes "fatter".

The compactness index  $C$  is defined to quantify the compactness of the patch shape. It is calculated as the ratio of the perimeter's square to the patch's area. In practice, it is calculated as the ratio of the square of the number of boundary pixels (including hole boundaries) to the total number of pixels in the patch (Figure 3b):

$$C = \frac{(N_{\text{edge}})^2}{N} \quad (4)$$

where  $N_{\text{edge}}$  represents the number of boundary pixels, and  $N$  is the total number of pixels in the patch. The compactness index  $C$  reflects the complexity of the patch's boundary and its shape compactness. As  $C$  approaches 1, the proportion of boundary pixels within the patch is relatively high, suggesting that the perimeter is longer and the shape may be more elongated or irregular. Conversely, as  $C$  approaches 0, the proportion of boundary pixels is smaller, indicating a shorter perimeter and a more compact and regular shape.

The convexity index  $S$  is defined to quantify the concavity/convexity of the patch. It is calculated as the ratio of the actual area of the patch to its convex hull area (Figure 3c):

$$S = \frac{A}{A_{\text{hull}}} \quad (5)$$

where  $A$  represents the actual area of the patch, which is the product of the number of non-zero pixels  $N$  and the square of the image resolution;  $A_{\text{hull}}$  represents the area of the convex hull, which is the smallest convex polygon that encloses the patch. The convex hull is computed using the convex hull algorithm, which calculates the smallest convex polygon that completely encloses the set of non-zero pixels. The area of this convex polygon is  $A_{\text{hull}}$ . When  $S$  approaches 1, it indicates that the patch shape is close to convex, with a more regular boundary. When  $S$  approaches 0, it indicates that the patch has a more complex shape with concavities or irregular edges.

The concavity index  $K$  is defined to further quantify the concavity of the patch and its internal complexity, which represents the proportion of holes in the total area after filling

the holes. In practice, it is calculated as the ratio of the number of hole pixels to the total number of pixels in the patch after the holes are filled (Figure 3d):

$$K = \frac{N_{\text{hole}}}{N_{\text{filled}}} \quad (6)$$

where  $N_{\text{hole}}$  represents the number of hole pixels, and  $N_{\text{filled}}$  represents the total number of pixels in the patch after the holes are filled. The concavity index reflects the relative scale of the holes within the patch. A higher value indicates that the patch contains more or larger holes, resulting in a more complex shape and a more irregular boundary.

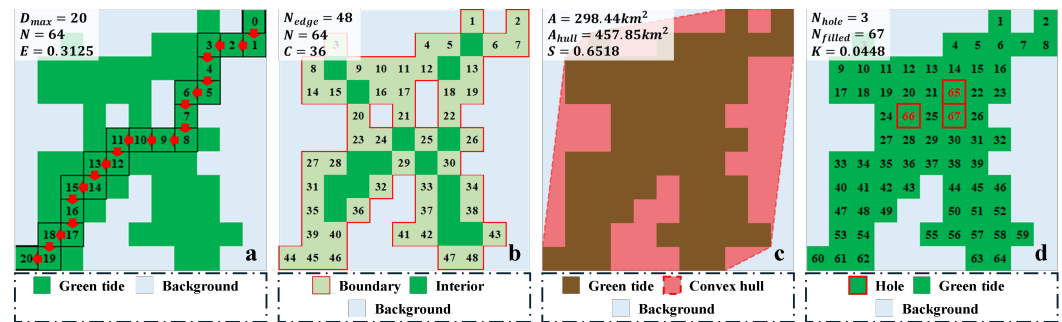


**Figure 3.** Schematic diagrams of patch elongation (a), compactness (b), convexity (c), and concavity (d) features.

## 2.5. Fractal Dimension

Fractal dimension (FD) is an index used to quantify the complexity and self-similarity of geometric shapes, reflecting the level of detail and spatial filling ability of an object at different scales [36]. The fractal dimension helps reveal patches' morphological complexity and spatial distribution patterns in studying patch morphological features. We used the box-counting method to calculate the fractal dimension of patches [37]. We performed preprocessing steps on the patch images, including orientation calculation, edge filling, and image rotation to a standard angle. These preprocessing steps are crucial for ensuring the accuracy and consistency of the fractal dimension calculation.

### 2.5.1. Box-Counting Method

The box-counting method estimates the fractal dimension  $F$  by covering the image at different scales and counting the boxes containing non-zero pixels. The box size  $\epsilon_i$  is selected as powers of 2, from the maximum to the minimum, so  $\epsilon_i$  is no larger than the image size:

$$\epsilon_i = 2^i \quad (7)$$

where  $i = (k, k-1, \dots, 1)$ , and  $k = \log_2 S$ . For each box size  $\epsilon_i$ , the image is divided into a grid with a size of  $\epsilon_i \times \epsilon_i$ , and the number of boxes containing non-zero pixels,  $N(\epsilon_i)$ , is counted. For each box size  $\epsilon_i$ , the values of  $\log_2 N(\epsilon)$  and  $\log_2 \left(\frac{1}{\epsilon}\right)$  are calculated and linearly fitted. The fractal dimension  $F$  is then obtained as the slope of the fitted line:

$$F = \frac{\Delta \log_2 N(\epsilon)}{\Delta \log_2 \left(\frac{1}{\epsilon}\right)} \quad (8)$$

where  $\Delta$  represents the increment of  $\log_2 N(\epsilon)$  or  $\log_2 \left(\frac{1}{\epsilon}\right)$  at different scales.

### 2.5.2. Orientation Calculation

First, it is necessary to determine the principal axis orientation of the binary image, which represents the primary direction of the patch's extension. Principal component analysis (PCA) is applied to analyze the coordinates of non-zero pixels in the binary image. Let the set of coordinates of non-zero pixels in the binary image be  $\{(x_i, y_i)\}_{i=1}^N$ , where  $N$  is the number of non-zero pixels. PCA is performed on all non-zero pixels to obtain the eigenvector  $u_1 = (u_{1,0}, u_{1,1})$  corresponding to the first principal component, which represents the direction of maximum variance in the data, i.e., the principal axis orientation  $\theta$ , calculated as follows:

$$\theta = \arctan 2(u_{1,0}, u_{1,1}) \quad (9)$$

where  $\theta$  is the calculated angle of the eigenvector  $u_1$  in the two-dimensional space relative to the origin. To ensure that the angle is measured from the positive  $x$ -axis ( $0^\circ$  in the eastward direction) and in the counterclockwise direction as positive, the value of  $\theta$  needs to be adjusted accordingly:

$$\theta' = (\theta \times \frac{180}{\pi} + 90) \bmod 360 \quad (10)$$

where  $\theta'$  represents the calculated orientation of the patch.

### 2.5.3. Image Rotation

In the box-counting method, we overlay grids of boxes with different scales on the image and count the number of boxes containing non-zero pixels. If the orientation of the image differs, the alignment of image features with the grid will also change, and this difference becomes more pronounced at larger scales. For example, when oriented diagonally, a line segment of the same length may pass through more boxes, while horizontally or vertically aligned line segments pass through fewer boxes. Therefore, different orientations can lead to variations in the box count, affecting the fractal dimension's calculation. Rotating the image to a consistent orientation can eliminate this orientation-induced variation. This study rotates all binary images to a standard  $45^\circ$  orientation (i.e., northeast direction). Nearest-neighbor interpolation is used during the rotation to maintain the binary characteristics of the image. By rotating all images to a uniform orientation, we can eliminate any bias in fractal dimension calculations caused by orientation differences, ensuring that the fractal dimension reflects the intrinsic complexity of the shape rather than the external influence of orientation.

### 2.5.4. Image Padding

To apply the box-counting method, the image dimensions must be powers of 2. This requirement arises because, during the box-counting process, the image must be divided evenly at different scales. When the image dimensions are powers of 2, the boxes can perfectly cover the image without leaving any residuals, simplifying the calculation and improving the accuracy of fractal dimension estimation. Therefore, the height  $H$  and width  $W$  are adjusted to the nearest power of 2 greater than or equal to their original dimensions to ensure that the image meets this requirement:

$$H_{\text{new}} = 2^{\lceil \log_2 H \rceil}, \quad W_{\text{new}} = 2^{\lceil \log_2 W \rceil} \quad (11)$$

where  $\lceil \cdot \rceil$  represents the ceiling function. Symmetric (or approximately symmetric) padding with a value of 0 is applied to the image's top, bottom, left, and right sides to minimize the impact of padding on the calculation results. Adjusting the image dimensions to the

nearest power of 2 ensures that the image can be evenly divided into an integer number of boxes at each box scale, avoiding generating residual areas. This adjustment allows for a more precise box-counting process and reduces errors caused by boundary effects.

### 2.5.5. Calculation of Fractal Dimension

Before calculating the fractal dimension, the patches need to be preprocessed. First, the patch orientation is calculated (Figure 4a) and rotated to a standard orientation of 45° (Figure 4b) to eliminate calculation biases caused by orientation differences. Then, the rotated image is padded (Figure 4c) to ensure that the image can be fully divided. Finally, the box-counting method is applied to calculate the fractal dimension  $F$  of each patch. As  $F$  approaches 1, it indicates that the patch shape is closer to a one-dimensional linear structure, similar to the elongation index, suggesting that the patch is more “slender”. As  $F$  approaches 2, it indicates that the patch shape is closer to a two-dimensional planar structure, suggesting the patch is “fatter”.

Figure 4d shows the box coverage effect when  $N_\epsilon = 32$  and the complete analysis of the fractal dimension calculation results. The result shows that the fractal dimension  $F$  of this patch is 1.2091, which is closer to 1. This value aligns with the patch’s elongated strip-like morphological feature, indicating a low spatial filling capacity, a simple boundary, and a lack of a complex fractal structure.

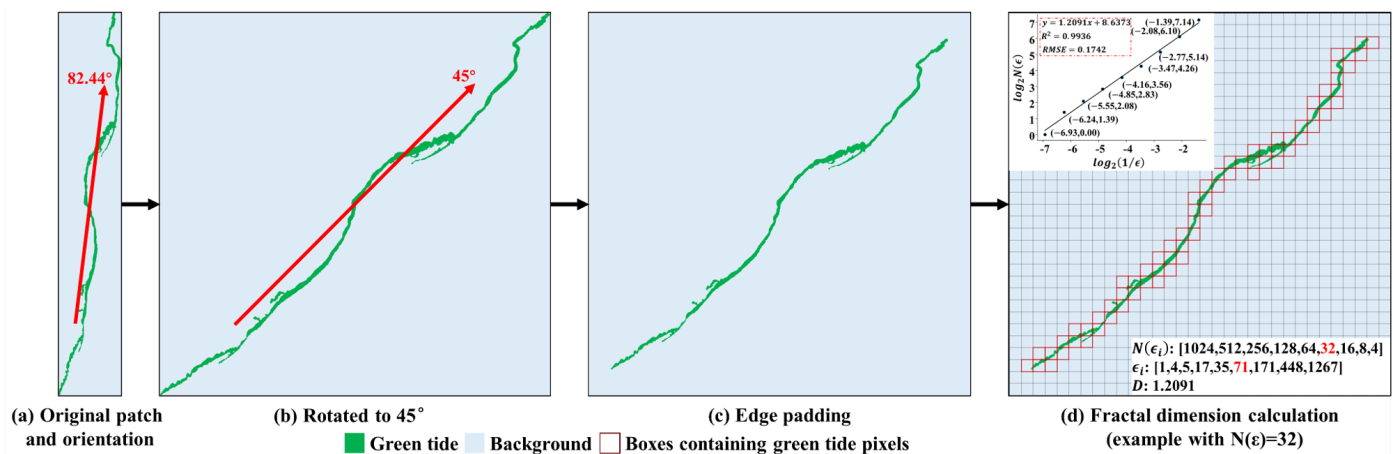


**Figure 4.** Process of calculating the fractal dimension of a patch.

### 2.6. Morphological Complexity

Morphological complexity (MC) is an index used to quantify the structural complexity of geometric shapes [38]. Skeletonization is an important morphological processing technique aimed at extracting the skeleton of a target object from a binary image. This process simplifies the shape representation while preserving the essential topological structure [39]. Through skeletonization, the target object is reduced to single-pixel-width lines, allowing the extraction of its primary geometric information without altering its connectivity and morphological characteristics. Thus, we applied this algorithm to assess the patches’ morphological complexity quantitatively.

The skeleton retains the fundamental shape features of the patch, so the ratio of skeleton length to patch area effectively quantifies morphological complexity. In practice, it is calculated as the ratio of the number of skeleton pixels to the total number of pixels in the patch (Figure 5):

$$W = \frac{L}{N} \quad (12)$$

where  $L$  represents the number of skeleton pixels, and  $N$  is the total number of pixels in the patch. A larger  $W$  value indicates that the skeleton length is relatively long compared to the patch area, suggesting that the patch has more complex morphological features, such as additional branches, extensions, and twists, making the shape more elongated or irregular. Conversely, a smaller  $W$  value indicates that the skeleton length is relatively short compared to the patch area, implying that the patch shape is more compact and regular, with a more straightforward structure.

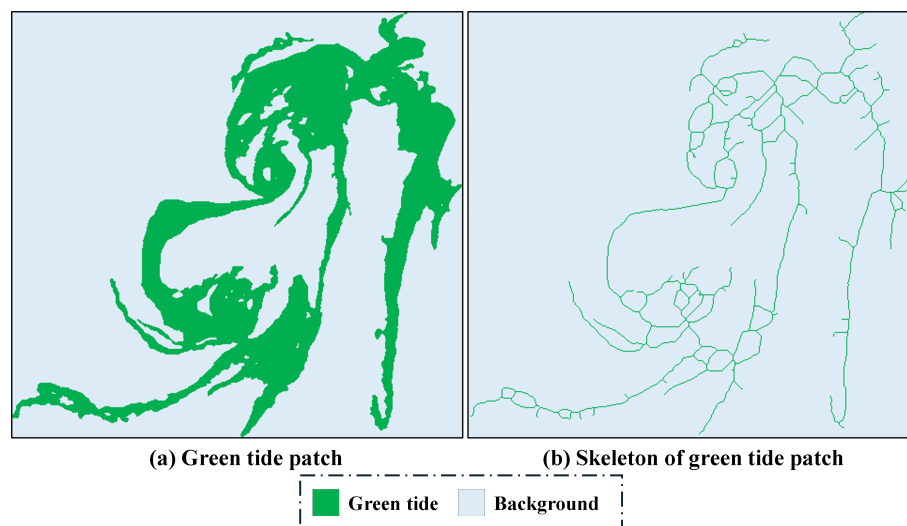


**Figure 5.** Schematic diagram of patch skeletonization.

### 2.7. Optimal Feature Selection

This study classified non-small patches into striped and non-striped types based on their morphology. Each patch's category is determined through manual interpretation, and the morphological features of each patch are calculated to conduct classification and analysis based on these morphological characteristics.

Before conducting patch classification research, we analyzed the data distribution, importance, and correlation between all morphological features, as shown in Figure 6. The results indicate that most features, including elongation, compactness, convexity, fractal dimension, and morphological complexity, follow a normal distribution, have an importance level above 10%, and exhibit some degree of correlation. In contrast, the concavity index performed poorly; its data distribution, importance, and correlation with other features were all suboptimal, with concavity values close to zero for most patches. This phenomenon aligns with the characteristics of the green tide. Before *Ulva prolifera* undergoes sufficient proliferation or striped patches merge into non-striped patches, it is difficult for internal holes to form, resulting in concavity values near zero. Based on this analysis, we ultimately selected elongation, compactness, convexity, fractal dimension, and morphological complexity as the five optimal features for classification to ensure accuracy and reliability.

### 2.8. Classification Based on Morphological Features

In terms of morphological features, smaller sizes and simpler edges characterize medium-sized patches compared to large patches, and the boundary between “striped” and “non-striped” forms is relatively indistinct. To ensure the generalization ability of the classification model and the objectivity of classification results, we conducted a morphology-based classification study separately for medium and large patches from the 1.04 million patch images. Data augmentation was applied through flipping and rotation to increase the number of training samples. Specifically, 25% of the samples were randomly selected for

data augmentation, and for the selected samples, four augmentation methods—randomly chosen from “vertical flip, horizontal flip, symmetric flip, rotation to 45°, rotation to 135°, rotation to 225°, and rotation to 315°”—were applied to ensure that the data augmentation did not significantly affect the sample distribution. The dataset was then divided into training, validation, and test sets in a 7:2:1 ratio. Several machine learning models, such as Random Forest, Support Vector Machine, and Logistic Regression, as well as deep learning models like MLP, CNN, and RNN, were selected for training. Accuracy, kappa coefficient, F1-score, and MIoU (mean intersection over union) were used to evaluate the classification accuracy of the models.

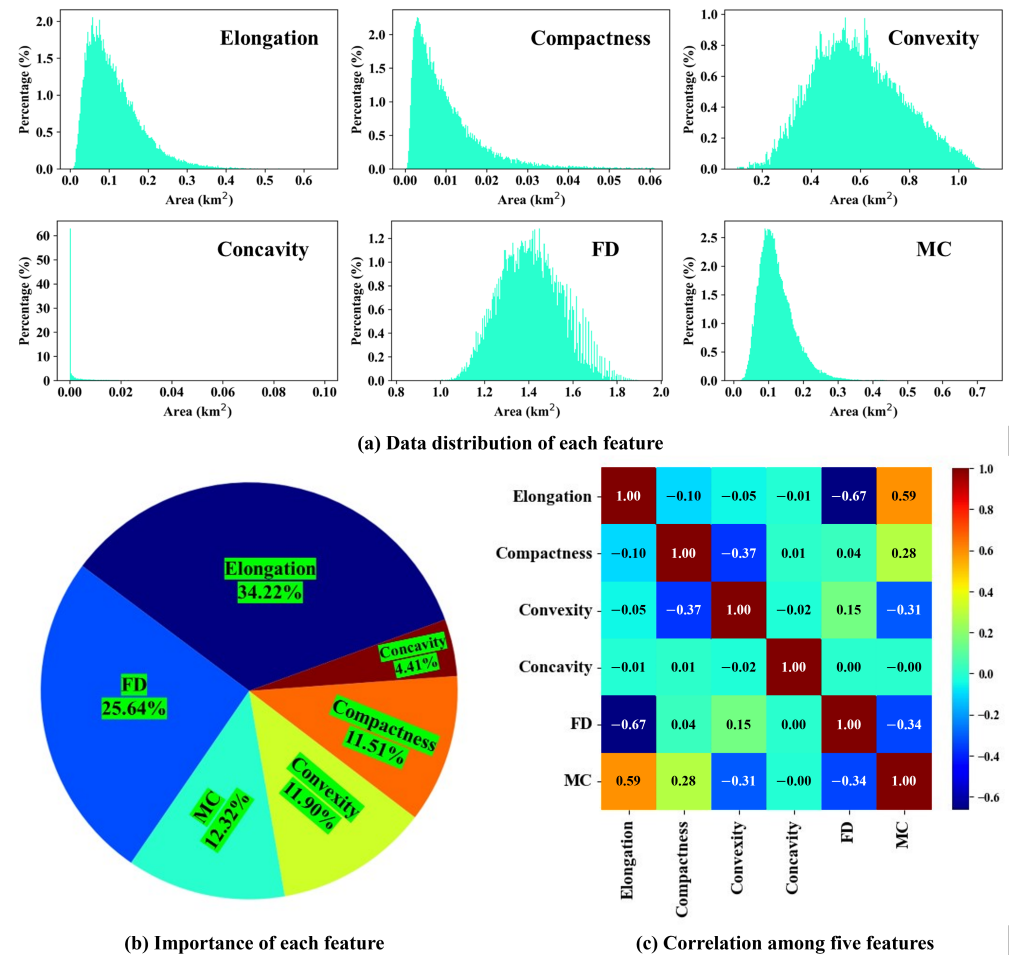


**Figure 6.** Data distribution (a), importance (b), and inter-feature correlation (c) of six morphological features.

The evaluation metrics are defined in Equations (13)–(18):

$$Accuracy = \frac{TP + TN}{TP + FP + TN + FN} \tag{13}$$

where  $TP$  is the number of true positives,  $TN$  is the number of true negatives,  $FP$  is the number of false positives, and  $FN$  is the number of false negatives. Accuracy measures the overall correctness of the classifier by evaluating the proportion of correct predictions.

$$\kappa = \frac{P_o - P_e}{1 - P_e} \tag{14}$$

where  $P_o$  is the observed accuracy and  $P_e$  is the expected accuracy. The kappa coefficient is used to measure the reliability of the classification results, especially in cases of class imbalance.

$$\text{Precision} = \frac{TP}{TP + FP} \quad (15)$$

Precision evaluates the proportion of predicted positive samples that are actually positive. A higher precision indicates that the classifier is more accurate in predicting positive cases.

$$\text{Recall} = \frac{TP}{TP + FN} \quad (16)$$

Recall measures the proportion of actual positive samples that are correctly identified as positive. A higher recall indicates that the classifier is capable of detecting a larger proportion of positive samples.

$$\text{F1-score} = \frac{2 \times \text{Precision} \times \text{Recall}}{\text{Precision} + \text{Recall}} \quad (17)$$

The F1-score is the harmonic mean of precision and recall, providing a single measure that balances both precision and recall.

$$\text{MIoU} = \frac{1}{C} \sum_{i=1}^C \frac{TP_i}{TP_i + FP_i + FN_i} \quad (18)$$

where  $C$  is the number of classes, and  $TP_i$ ,  $FP_i$ , and  $FN_i$  represent the true positives, false positives, and false negatives for the  $i$ -th class. MIoU (mean intersection over union) is a common evaluation metric in segmentation tasks, which measures the accuracy of predictions for each class by considering both the true positive rate and the error rate.

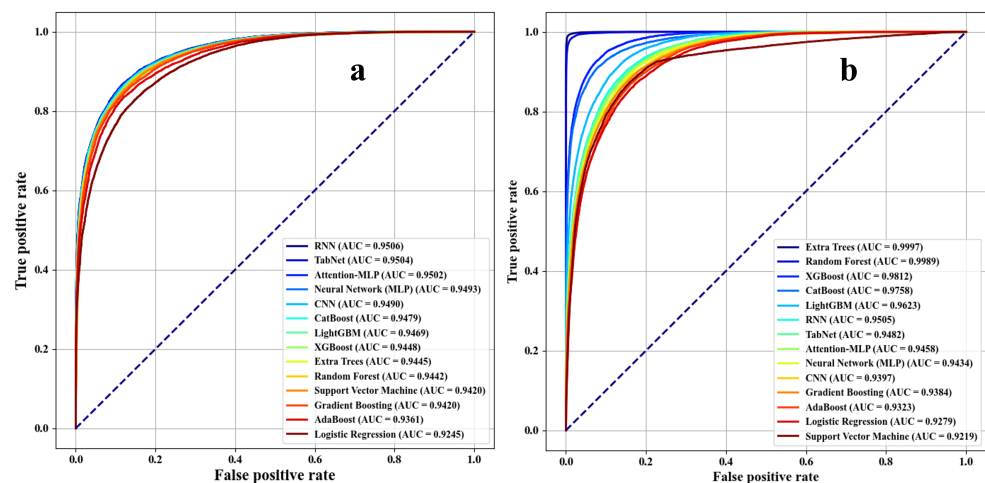
The evaluation results for classification accuracy across models are shown in Table 2. The results indicate that the Extra Trees model, with 100 estimators, and the Random Forest model performed exceptionally well overall, demonstrating high accuracy, kappa coefficient, F1-score, and MIoU values for both medium and large patches. Specifically, the Extra Trees model achieved outstanding performance on large patches, with an accuracy of 0.9844, a kappa coefficient of 0.9629, an F1-score of 0.9844, and an MIoU of 0.9637. The Multi-Layer Perceptron (MLP), configured with a hidden layer size of 100 units and a maximum of 500 iterations, exhibited strong performance on medium patches, with an accuracy of 0.8763, along with high F1-score and MIoU values. CatBoost also demonstrated a balanced performance across all metrics on medium patches. In comparison, Logistic Regression and AdaBoost yielded slightly lower performance but still maintained reasonable classification ability. Overall, all models performed better on large patches than on medium patches, with ensemble models such as Extra Trees and Random Forest yielding notably superior results.

To further assess model performance, 10-fold cross-validation was used to calculate each model's AUC (area under the curve) values on medium and large patches. The ROC (receiver operating characteristic) curves for each model are shown in Figure 7. The ROC curve is a graphical representation of the trade-off between the true positive rate (TPR) and false positive rate (FPR) at various classification thresholds. The TPR, also known as sensitivity or recall, is defined as follows:

$$\text{TPR} = \frac{TP}{TP + FN} \quad (19)$$

**Table 2.** Evaluation results of classification accuracy for each model.

Model	Accuracy		Kappa Coefficient		F1-Score		MIoU	
	Medium	Large	Medium	Large	Medium	Large	Medium	Large
Random Forest	0.8659	0.9773	0.7174	0.9457	0.8660	0.9772	0.7538	0.9474
Support Vector Machine	0.8656	0.8643	0.7147	0.6692	0.8652	0.8620	0.7519	0.7221
Logistic Regression	0.8401	0.8574	0.6586	0.6562	0.8390	0.8559	0.7106	0.7128
Gradient Boosting	0.8599	0.8681	0.7035	0.6816	0.8597	0.8666	0.7434	0.7308
Decision Tree	0.8122	0.9548	0.6057	0.8928	0.8126	0.9547	0.6728	0.8990
Extra Trees	0.8693	0.9844	0.7240	0.9629	0.8692	0.9844	0.7589	0.9637
K-Nearest Neighbors	0.8562	0.9368	0.6962	0.8497	0.8561	0.9366	0.7379	0.8616
XGBoost	0.8669	0.9255	0.7198	0.8212	0.8671	0.9249	0.7556	0.8379
CatBoost	0.8716	0.9178	0.7294	0.8023	0.8717	0.9170	0.7629	0.8225
AdaBoost	0.8545	0.8544	0.6911	0.6481	0.8540	0.8526	0.7342	0.7072
LightGBM	0.8669	0.8945	0.7197	0.7197	0.8670	0.8935	0.7555	0.7786
Neural Network (MLP)	0.8763	0.8720	0.7393	0.6923	0.8764	0.8709	0.7706	0.7385
Attention-MLP	0.8737	0.8748	0.7325	0.7000	0.8734	0.8739	0.7654	0.7440
TabNet	0.8757	0.8805	0.7372	0.7116	0.8755	0.8791	0.7690	0.7526
CNN	0.8726	0.8694	0.7298	0.6844	0.8723	0.8678	0.7634	0.7329
RNN	0.8730	0.8801	0.7319	0.7127	0.8729	0.8792	0.7649	0.7533
Average Value	0.8625	0.9008	0.7094	0.7594	0.8624	0.8998	0.7482	0.7941

**Figure 7.** ROC curves of each model for medium (a) and large (b) patches. Since the Decision Tree model typically outputs discrete classification results rather than continuous probabilities, its ROC curve appears as a simple triangle in this study; therefore, the ROC curve for the decision tree model was not plotted.

The FPR is defined as follows:

$$\text{FPR} = \frac{FP}{FP + TN} \quad (20)$$

The ROC curve is plotted by varying the decision threshold, and the curve represents the trade-off between TPR and FPR across different thresholds. The AUC is the area under the ROC curve, providing a scalar value that summarizes the performance of the classification model. The AUC value ranges from 0 to 1, with a higher value indicating better model performance. AUC can be calculated as follows:

$$\text{AUC} = \int_0^1 \text{TPR}(\text{FPR}) d\text{FPR} \quad (21)$$

An AUC of 0.5 indicates a model with no discriminative power (i.e., random guessing), while an AUC of 1.0 indicates perfect classification performance.

The results show that RNN, TabNet, and Attention-MLP performed well on medium patches, with AUC values reaching 0.9506, 0.9504, and 0.9502, respectively. Extra Trees and Random Forest achieved near-perfect AUC values of 0.9997 and 0.9989 on large patches, demonstrating extremely high recognition ability for large patches. Ensemble models outperformed traditional linear models on medium and large patches, with a particularly pronounced advantage on large patches.

Considering the classification performance of each model, the morphological features proposed in this study, such as elongation and fractal dimension, have demonstrated significant effectiveness in patch classification, especially when combined with ensemble models like Extra Trees and Random Forest. Through a comparative analysis of medium and large patches, the classification effectiveness of each feature across different scales was validated, confirming the utility and applicability of these morphological features in patch classification tasks. This provides a basis for further assessing the impact of patches with different morphologies on the scale effects.

### 3. Results

Based on the size and morphological features of green tide patches, the patches were classified into five types: small, medium-striped, medium-non-striped, large-striped, and large-non-striped. The impact of each type on the scale effects was then evaluated. Patches at a 16 m resolution were used as the baseline, and integer multiples of 16 m were applied for resampling to generate images with resolutions ranging from 32 m to 256 m. The actual area of each patch was estimated by multiplying the square of the resolution by the number of patch pixels, simulating the detection performance of the same patch at different resolutions.

The resampling was conducted using a block-aggregation-based vectorization strategy [40]. The original binary image was cropped to match the specified scaling factor and then resized into a series of matrix blocks corresponding to the scaling factor [41]. The average proportion of target pixels within each block was calculated, and a specific threshold was set to classify each low-resolution pixel, thus determining its value [42]. This method preserves as many of the key morphological features of the patches as possible. A fitting analysis was performed on the resampled patch areas compared to the baseline area, evaluating the detection performance of patches with different morphologies and sizes at each resolution to explore the correlation between patch morphology and the scale effects.

#### 3.1. Striped Type

The resampling area fitting results for striped patches are shown in Figure 8. As the resolution decreases, the area fitting's linearity coefficient ( $R^2$ ) gradually decreases, and the root mean square error ( $RMSE$ ) progressively increases, indicating that the accuracy of area estimation for striped patches declines significantly at lower resolutions. Specifically, for large-striped patches at a resolution of 32 m, the fitting equation is  $y = 0.9371x - 0.0396$  (Figure 8a), with an  $R^2$  of 0.999 and an  $RMSE$  of 0.0417 (Figure 8c), indicating a high accuracy in area estimation. However, when the resolution is reduced to 256 m, the slope of the fit decreases significantly to 0.5367,  $R^2$  drops to 0.8902, and  $RMSE$  increases to 0.2602. These results indicate that striped patches are sensitive to the scale effects at lower resolutions, as their elongated shape tends to lose detail at coarser scales, leading to increased area estimation error. The linear extensibility of the striped structure makes it difficult for low-resolution pixels in block aggregation to fully retain the strip's elongation, resulting in notable area errors.

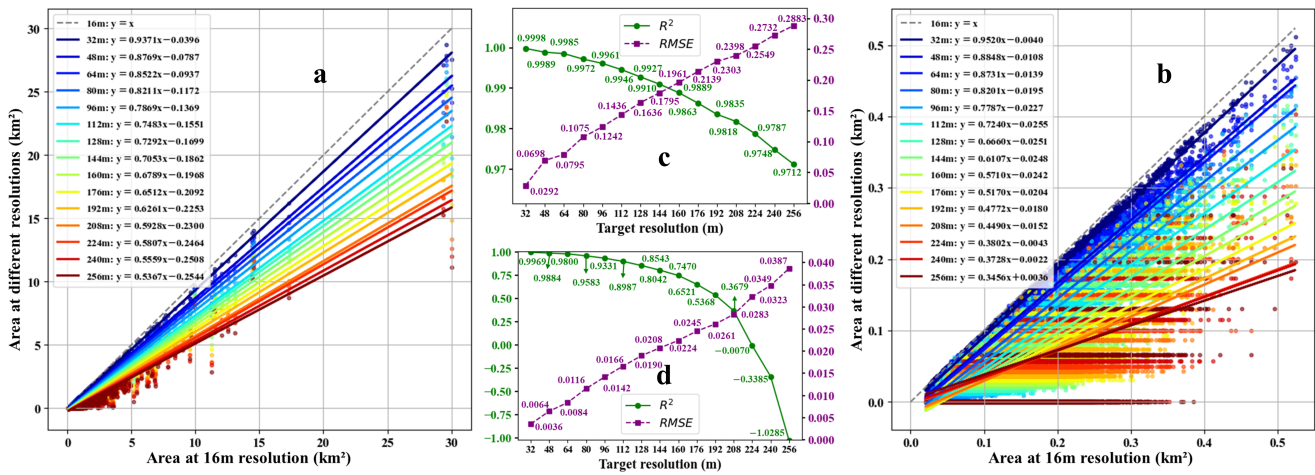


**Figure 8.** Area fitting results for large (a) and medium (b) striped patches and fitting evaluation metrics ( $R^2$  and RMSE) for large (c) and medium (d) striped patches.

Medium-striped patches exhibit an even more pronounced loss of accuracy as the resolution decreases. At a resolution of 32 m, the fitting equation is  $y = 0.9520x - 0.0040$  (Figure 8b), with an  $R^2$  of 0.9969 and an RMSE of only 0.0036 (Figure 8d), indicating that the resampled area closely approximates the baseline area. However, as the resolution decreases to 256 m, the slope of the fitting equation drops sharply to 0.3456, and  $R^2$  takes on negative values ( $R^2$  values for 224 m, 240 m, and 256 m resolutions are  $-0.0070$ ,  $-0.3385$ , and  $-1.0285$ , respectively, in Figure 8d), with RMSE increasing to 0.0387. Negative  $R^2$  values indicate a lack of linear relationship in area fitting, with resampled areas significantly deviating from the actual values. This area estimation error is due to the elongated shape of medium-striped patches, which tends to be masked by low-resolution pixel aggregation at coarse scales, resulting in the loss of strip characteristics.

The area fitting results after resampling reveal variations in signal strength for striped patches of different sizes across resolutions. In practical applications, medium-striped patches have high signal strength in high-resolution images (e.g., 16 m and 32 m) due to their linear solid extensibility, making them detectable by remote sensing algorithms. However, as the resolution decreases, the signal strength of medium-striped patches weakens significantly or even disappears in low-resolution images, causing some patches to have zero area at lower resolutions, thus exhibiting a significant scale effect. This area loss phenomenon reflects the difficulty in detecting striped patches in low-resolution images, highlighting the high sensitivity of striped patches to the scale effects.

### 3.2. Non-Striped Type

The resampled area fitting results for non-striped patches are shown in Figure 9. In contrast, the fitting accuracy of large-non-striped patches demonstrates higher stability as the resolution decreases. At a resolution of 32 m, the fitting equation is  $y = 0.9754x - 0.0192$ , with an  $R^2$  of 0.9998 and an RMSE of 0.0292, which greatly agrees with the reference area. When the resolution is reduced to 256 m, the fitting slope slightly decreases to 0.7470, while the  $R^2$  remains at 0.9713 and the RMSE increases to 0.2883. Although there is some error in area estimation at lower resolutions, the fitting accuracy for large-non-striped patches remains relatively stable. This stability can be attributed to the compact and homogeneous morphology of non-striped patches, which retain their structural and area characteristics well even at a resolution of 256 m, effectively preventing area loss due to reduced resolution. This characteristic allows for relatively accurate monitoring results for non-striped patches at low-resolution images, with area estimation less affected by scale effects.

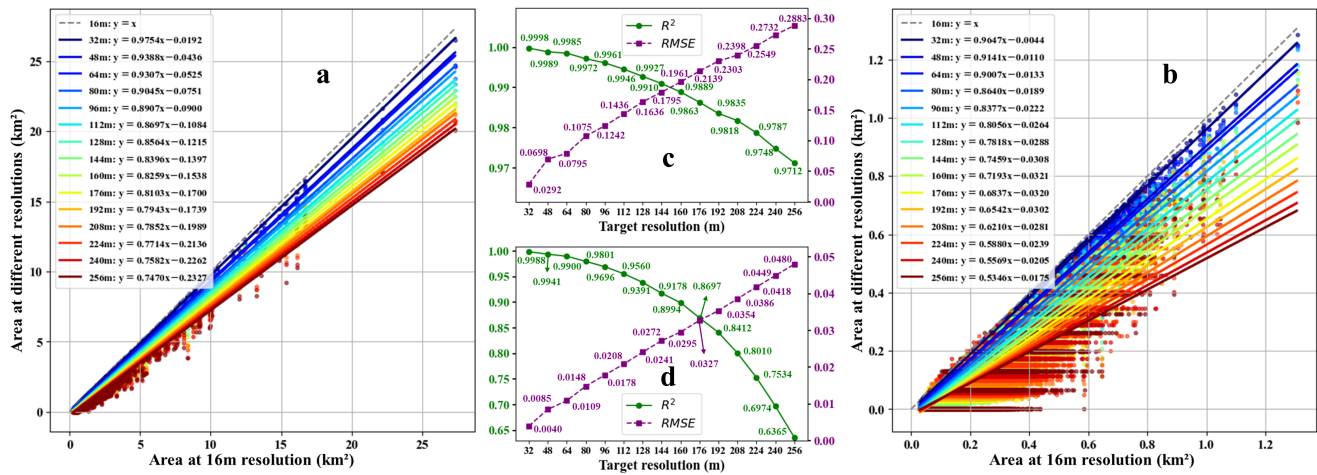


**Figure 9.** Area fitting results for large (a) and medium (b) non-striped patches and fitting evaluation metrics ( $R^2$  and RMSE) for large (c) and medium (d) non-striped patches.

For medium-non-striped patches, although the resolution reduction similarly leads to a decrease in fitting accuracy, the change is more gradual. At a resolution of 32 m, the fitting equation is  $y = 0.9647x - 0.0044$ , with an  $R^2$  of 0.9988 and an RMSE of 0.0040, indicating high accuracy in area estimation. However, when the resolution is reduced to 256 m, the fitting slope decreases to 0.5346, the  $R^2$  drops to 0.6365, and the RMSE increases to 0.0480. These results suggest that medium-non-striped patches are less sensitive to scale effects than striped patches. While medium-non-striped patches have higher signal strength in high-resolution images, there is a slight signal attenuation in low-resolution images, leading to a minor impact on area estimation accuracy. This signal attenuation is particularly pronounced in medium-non-striped patches, indicating that even compactly structured patches face some scale effects in multi-scale detection.

### 3.3. Small Type

The distribution of resampled area data points for small patches is shown in Figure 10a. It illustrates that for most resolutions, different reference areas correspond to similar resampled areas, indicating that the linear relationship between the resampled area and reference area has been significantly lost. Additionally, many data points lie above the standard fitting line  $y = x$ , suggesting that small patches exhibit both overestimation and underestimation in scale effects, with overestimation being more common than other patch types. Figure 10b shows the change in the proportion of patches with a resampled area of zero as the target resolution decreases. During the resolution reduction process, many patches have their area reduced to zero, meaning that the detection signal for these patches completely disappears in low-resolution imagery, which is one of the critical causes of scale effects.

Figure 10c presents the variation in the ratio of resampled area to baseline area as resolution decreases. It can be observed that as the resolution reduces, the proportion of retained area decreases for all patch types, indicating an increasing loss of green tide coverage. The rate of area loss varies among patch categories. Small patches experience the most pronounced loss, with their resampled area-to-baseline area ratio rapidly declining, highlighting their susceptibility to underrepresentation in lower resolutions. Medium and large patches also exhibit area loss, but the decline is relatively more moderate, with non-striped patches generally retaining a higher proportion of their area compared to striped ones. This trend underscores the increasing difficulty of accurately detecting and characterizing green tide patches at coarser resolutions, emphasizing the scale effects and their impact on detection reliability.

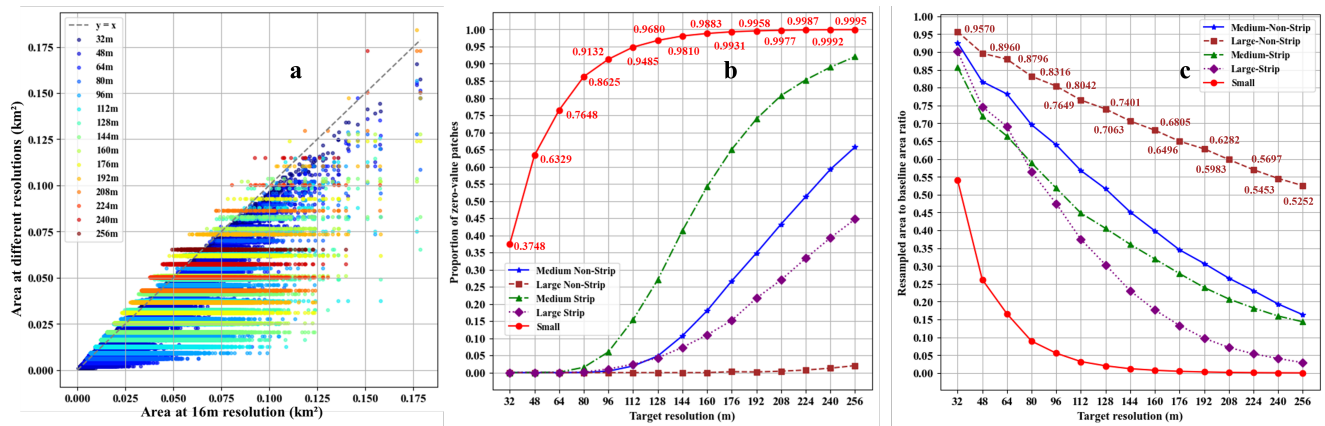


**Figure 10.** (a) Scatter plot of resampled area for small patches. (b) Change in the proportion of patches with a resampled area of zero across different patch types as the target resolution decreases. (c) Change in the ratio of the resampled area to the baseline area across different patch types as the target resolution decreases. The data points for patches with a resampled area of zero at multiple resolutions are not displayed in (a) due to significant overlap.

There is a significant difference in the scale effects between striped and non-striped patches. Striped patches, especially medium-striped ones, are highly sensitive to resolution changes due to their linear, elongated morphology, which leads to severe signal attenuation, area estimation deviations, or even complete loss of detection at coarser scales. In contrast, non-striped patches, with their compact structure, maintain relatively high signal strength and area estimation accuracy even in low-resolution imagery. Small patches, inherently smaller in area, are more prone to signal loss and misestimation in low-resolution images, often disappearing entirely during the downscaling process. This makes the scale effects for small patches more complex and pronounced compared to medium-striped or large-non-striped patches.

## 4. Discussion

### 4.1. Scale Effects and Morphological Sensitivity of Green Tide Patches

As shown in Figure 11, the impact of scale effects on green tide patches with different morphologies varies significantly. By constructing resampling area fitting equations for medium and large patches, we found that these equations demonstrate higher reliability for area estimation of large-non-striped patches. The patches maintain good distinguishability across different resolutions (Figure 11(a1–a16)), indicating that changes in scale have minimal influence on the morphological characteristics of large-non-striped patches. In contrast, the linearity of the fitting equations for medium patches decreases with size reduction, while small patches almost entirely lose their linear relationship. This finding suggests that medium and small patches are more sensitive to resolution changes, resulting in significant errors in area estimation. Furthermore, striped patches exhibit better detection performance in high-resolution imagery, but when the resolution decreases, they tend to fragment into small strips or isolated patches. As shown in Figure 11(b3–b16), patches are divided into multiple parts, losing connectivity. The existing fitting equations fail to map green tide areas in low-resolution imagery accurately.

In practical green tide monitoring tasks, data resolution is often inversely proportional to the satellite's swath width and revisit cycle. Therefore, obtaining long-term and large-scale monitoring results requires synergistic observations from multi-source satellite data. However, the actual morphological characteristics of green tide patches can typically be accurately identified only in high-resolution imagery. For example, Figure 11(b1) illustrates a distinct striped patch at a 16 m resolution. However, as the resolution decreases, the

detection results degrade into several small patches, which makes estimating the 16 m resolution area using existing fitting equations at lower resolutions challenging. This outcome highlights the irreversibility of the area-fitting equations and reflects the limitations of the proposed method.

Based on these findings, we believe that effectively incorporating morphological features into multi-source remote sensing data can further enhance the accuracy and stability of green tide monitoring. Specifically, the differential responses of patches with varying morphologies to scale effects suggest more robust algorithms addressing the high-scale sensitivity of striped and small patches in multi-scale data fusion. Such improvements will contribute to better spatial characterization of green tide dynamics, especially in multi-source data environments with inconsistent resolutions. They will more accurately reflect the actual distribution of green tides.

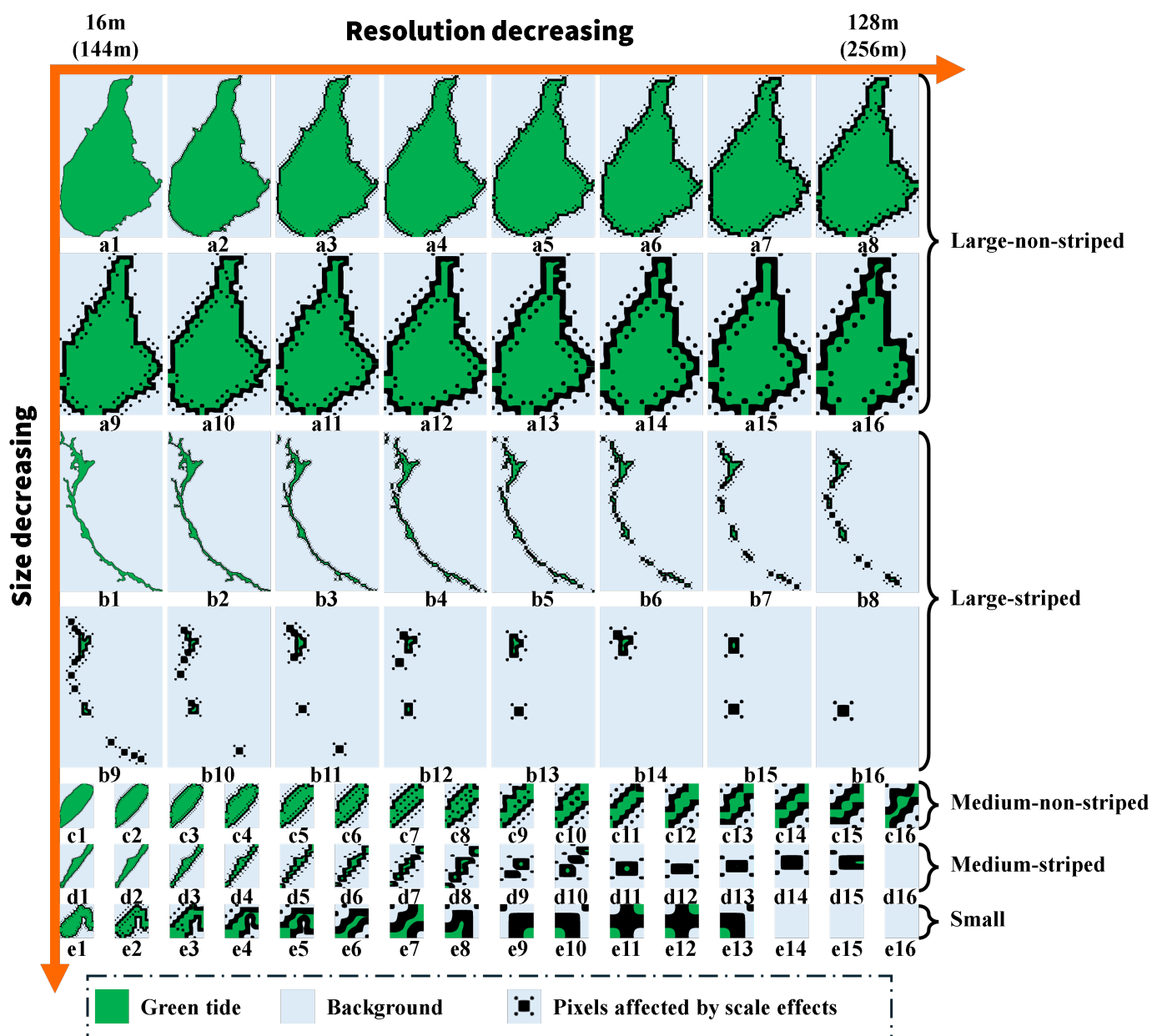


Figure 11. Morphological changes of five types of patches as the resolution decreases, including large-non-striped (a1–a16), large-striped (b1–b16), medium-non-striped (c1–c16), medium-striped (d1–d16), small (e1–e16).

#### 4.2. Potential of Super-Resolution Methods in Green Tide Area Estimation

The limitations of area estimation at low resolutions, as highlighted in our findings, suggest that super-resolution methods could be a promising approach to address these challenges. Super-resolution techniques, which aim to reconstruct high-resolution images from low-resolution data, have shown significant potential in enhancing spatial detail and improving feature detection in various remote sensing applications. By applying super-resolution algorithms, such as convolutional neural networks (e.g., SRCNN [43]) or generative adversarial networks (e.g., SRGAN [44,45]), the spatial resolution of low-resolution imagery could be effectively enhanced, potentially mitigating the loss of morphological detail and improving the reliability of green tide area estimation.

For instance, super-resolution methods could help preserve the connectivity and structural integrity of striped patches, which tend to fragment into smaller parts as resolution decreases. This would enable more accurate area estimation and morphological analysis, even in imagery with coarser resolutions. Similarly, small patches that are particularly sensitive to resolution changes might retain their detectable area proportions through enhanced spatial detail provided by super-resolution techniques, thereby reducing the proportion of zero-value patches.

Despite these advantages, the practical application of super-resolution methods in green tide monitoring presents challenges. These include the computational cost of processing large-scale datasets, the potential introduction of artifacts during reconstruction, and the need for high-quality training data to ensure robust model performance. Additionally, the effectiveness of super-resolution methods in preserving the spectral and morphological fidelity of green tide patches across multi-source remote sensing datasets requires further investigation.

Nevertheless, integrating super-resolution techniques into existing area estimation workflows could complement the proposed methods by improving the spatial characterization of green tides in low-resolution imagery. Future work should explore the feasibility and effectiveness of super-resolution approaches for green tide monitoring, particularly in multi-scale and multi-source data fusion scenarios. This could enhance the accuracy and reliability of green tide area estimation, offering valuable insights into their spatial and temporal dynamics.

## 5. Conclusions

This study systematically investigated the impact of morphological characteristics of green tide patches on scale effects in area estimation. First, green tides were detected using the VB-FAH index based on GF-1 WFV data, and patch regions were segmented and extracted using the CCL algorithm. The extracted patches were then categorized by size into small, medium, and large patches. Next, morphological features such as elongation, compactness, convexity, fractal dimension, and morphological complexity were introduced to construct machine learning models, enabling accurate classification of striped and non-striped patches. Finally, resampling simulations at various resolutions were performed to analyze changes in area estimation for patches of different sizes and morphologies as resolution decreased, resulting in the derivation of fitting equations between the baseline area and the resampled area. The results showed that area estimation for large patches remained relatively stable across resolution changes. In contrast, the errors in area estimation for medium and small patches increased as resolution significantly decreased. Striped patches, mainly, were more sensitive to scale effects, exhibiting greater deviations in area estimation under low-resolution imagery and partial irreversibility in the fitting equations. This phenomenon highlights the critical role of size and morphological

features in green tide area estimation. It emphasizes incorporating patch morphology in multi-source remote sensing monitoring to enhance accuracy.

Future work should prioritize enhancing morphological feature extraction and classification algorithms to improve the detection and characterization of green tide dynamics. Advanced methods, such as deep-learning-based shape descriptors and attention mechanisms, could better capture subtle morphological variations, particularly for small and fragmented patches, thereby mitigating the scale effects observed in area estimation. Furthermore, integrating these enhanced algorithms into multi-scale monitoring frameworks would allow for more consistent and accurate representation of green tide dynamics across varying resolutions. Additionally, the prospective application of these advancements in early warning systems for green tide outbreaks deserves further investigation. By leveraging enhanced morphological features and improved classification algorithms, such systems could provide timely and reliable predictions, aiding in the mitigation of green tide impacts on coastal environments. In the future, developing robust area estimation models tailored to different morphological types, combined with multi-source and multi-scale monitoring data, will significantly improve the spatial representation of green tide dynamics and support the effective management of green tide events.

**Author Contributions:** Conceptualization, K.W. and T.X.; methodology, K.W. and T.X.; validation, K.W., T.X., J.L. and C.W.; formal analysis, K.W. and T.X.; investigation, K.W.; writing—original draft preparation, K.W. and T.X.; writing—review and editing, T.X., J.L., X.Z., H.L. and S.B.; visualization, K.W.; funding acquisition, T.X. All authors have read and agreed to the published version of the manuscript.

**Funding:** This research was funded by National Key Research and Development Program of China (grant no. 2022YFC3004200).

**Data Availability Statement:** The GF-1 WFV data were obtained from the China Resource Satellite Application Center (<https://data.cresda.cn/>, accessed on 20 September 2024).

**Acknowledgments:** The authors would like to acknowledge the China Resource Satellite Application Center for providing the GF-1 WFV data used in this study (<https://data.cresda.cn/>, accessed on 20 September 2024).

**Conflicts of Interest:** The authors declare no conflicts of interest.

## References

1. Xia, Z.; Liu, J.; Zhao, S.; Sun, Y.; Cui, Q.; Wu, L.; Gao, S.; Zhang, J.; He, P. Review of the development of the green tide and the process of control in the southern Yellow Sea in 2022. *Estuar. Coast. Shelf Sci.* **2024**, *302*, 108772. [[CrossRef](#)]
2. Feng, G.; Zeng, Y.; Wang, J.; Dai, W.; Bi, F.; He, P.; Zhang, J. A bibliometric review of Green Tide research between 1995–2023. *Mar. Pollut. Bull.* **2024**, *208*, 116941. [[CrossRef](#)] [[PubMed](#)]
3. Ji, M.; Dou, X.; Zhao, C.; Zhu, J. Exploring the Green Tide Transport Mechanisms and Evaluating Leeway Coefficient Estimation via Moderate-Resolution Geostationary Images. *Remote Sens.* **2024**, *16*, 2934. [[CrossRef](#)]
4. Hu, C.; Qi, L.; Hu, L.; Cui, T.; Xing, Q.; He, M.; Wang, N.; Xiao, Y.; Sun, D.; Lu, Y.; et al. Mapping *Ulva prolifera* green tides from space: A revisit on algorithm design and data products. *Int. J. Appl. Earth Obs. Geoinf.* **2023**, *116*, 103173. [[CrossRef](#)]
5. Park, J.; Lee, H.; De Saeger, J.; Depuydt, S.; Asselman, J.; Janssen, C.; Heynderickx, P.M.; Wu, D.; Ronsse, F.; Tack, F.M.G.; et al. Harnessing green tide *Ulva* biomass for carbon dioxide sequestration. *Rev. Environ. Sci. Biotechnol.* **2024**, *23*, 1041–1061. [[CrossRef](#)]
6. Tian, W.; Wang, J.; Zhang, F.; Liu, X.; Yang, J.; Yuan, J.; Mi, X.; Shao, Y. The Detection of Green Tide Biomass by Remote Sensing Images and In Situ Measurement in the Yellow Sea of China. *Remote Sens.* **2023**, *15*, 3625. [[CrossRef](#)]
7. Ding, Y.; Gao, S.; Huang, G.; Wu, L.; Wang, Z.; Yuan, C.; Yu, Z. A Novel Method for Simplifying the Distribution Envelope of Green Tide for Fast Drift Prediction in the Yellow Sea, China. *Remote Sens.* **2024**, *16*, 3520. [[CrossRef](#)]
8. Xia, Z.; Yang, Y.; Zeng, Y.; Sun, Y.; Cui, Q.; Chen, Z.; Liu, J.; Zhang, J.; He, P. Temporal succession of micropropagules during accumulation and dissipation of green tide algae: A case study in Rudong coast, Jiangsu Province. *Mar. Environ. Res.* **2024**, *202*, 106719. [[CrossRef](#)] [[PubMed](#)]

9. Shang, Y.; Jiang, L.; Wang, L.; Ye, Z.; Gao, S.; Tang, X. Methods for detecting green tide in the Yellow Sea using Google Earth Engine platform. *Reg. Stud. Mar. Sci.* **2024**, *77*, 103666. [\[CrossRef\]](#)
10. Hu, C.; He, M.-X. Origin and Offshore Extent of Floating Algae in Olympic Sailing Area. *Eos, Trans. Am. Geophys. Union* **2008**, *89*, 302–303. [\[CrossRef\]](#)
11. Hou, W.; Chen, J.; He, M.; Ren, S.; Fang, L.; Wang, C.; Jiang, P.; Wang, W. Evolutionary trends and analysis of the driving factors of *Ulva prolifera* green tides: A study based on the random forest algorithm and multisource remote sensing images. *Mar. Environ. Res.* **2024**, *198*, 106495. [\[CrossRef\]](#) [\[PubMed\]](#)
12. Keesing, J.K.; Liu, D.; Fearn, P.; Garcia, R. Inter- and intra-annual patterns of *Ulva prolifera* green tides in the Yellow Sea during 2007–2009, their origin and relationship to the expansion of coastal seaweed aquaculture in China. *Mar. Pollut. Bull.* **2011**, *62*, 1169–1182. [\[CrossRef\]](#) [\[PubMed\]](#)
13. Garcia, R.A.; Fearn, P.; Keesing, J.K.; Liu, D. Quantification of floating macroalgae blooms using the scaled algae index. *J. Geophys. Res. Oceans* **2013**, *118*, 26–42. [\[CrossRef\]](#)
14. Hu, C. A novel ocean color index to detect floating algae in the global oceans. *Remote Sens. Environ.* **2009**, *113*, 2118–2129. [\[CrossRef\]](#)
15. Xing, Q.; Hu, C. Mapping macroalgal blooms in the Yellow Sea and East China Sea using HJ-1 and Landsat data: Application of a virtual baseline reflectance height technique. *Remote Sens. Environ.* **2016**, *178*, 113–126. [\[CrossRef\]](#)
16. Shang, W.; Gao, Z.; Gao, M.; Jiang, X. Monitoring Green Tide in the Yellow Sea Using High-Resolution Imagery and Deep Learning. *Remote Sens.* **2023**, *15*, 1101. [\[CrossRef\]](#)
17. Wang, Z.; Fan, B.; Yu, D.; Fan, Y.; An, D.; Pan, S. Monitoring the Spatio-Temporal Distribution of *Ulva prolifera* in the Yellow Sea (2020–2022) Based on Satellite Remote Sensing. *Remote Sens.* **2023**, *15*, 157. [\[CrossRef\]](#)
18. Guo, Y.; Gao, L.; Li, X. A Deep Learning Model for Green Algae Detection on SAR Images. *IEEE Trans. Geosci. Remote Sens.* **2022**, *60*, 1–14. [\[CrossRef\]](#)
19. Cui, B.; Liu, M.; Chen, R.; Zhang, H.; Zhang, X. Anisotropic Green Tide Patch Information Extraction Based on Deformable Convolution. *Remote Sens.* **2024**, *16*, 1162. [\[CrossRef\]](#)
20. Xu, M.; Zhu, X.; Liu, Y.; Liu, S.; Sheng, H. A multi-scale context-aware and batch-independent lightweight network for green tide extraction from SAR images. *Int. J. Remote Sens.* **2024**, *45*, 4474–4499. [\[CrossRef\]](#)
21. Cui, B.; Zhang, H.; Jing, W.; Liu, H.; Cui, J. SRSe-Net: Super-Resolution-Based Semantic Segmentation Network for Green Tide Extraction. *Remote Sens.* **2022**, *14*, 710. [\[CrossRef\]](#)
22. Cao, Y.; Wu, Y.; Fang, Z.; Cui, X.; Liang, J.; Song, X. Spatiotemporal Patterns and Morphological Characteristics of *Ulva prolifera* Distribution in the Yellow Sea, China in 2016–2018. *Remote Sens.* **2019**, *11*, 445. [\[CrossRef\]](#)
23. Wang, Z.; Fang, Z.; Liang, J.; Song, X. Estimating *Ulva prolifera* green tides of the Yellow Sea through ConvLSTM data fusion. *Environ. Pollut.* **2023**, *324*, 121350. [\[CrossRef\]](#)
24. Xu, S.; Yu, T.; Xu, J.; Pan, X.; Shao, W.; Zuo, J.; Yu, Y. Monitoring and Forecasting Green Tide in the Yellow Sea Using Satellite Imagery. *Remote Sens.* **2023**, *15*, 2196. [\[CrossRef\]](#)
25. Hu, C.; Lee, Z.; Ma, R.; Yu, K.; Li, D.; Shang, S. MODIS Observations of Cyanobacteria Blooms in Taihu Lake, China. *J. Geophys. Res. Oceans* **2010**, *115*, C4. [\[CrossRef\]](#)
26. Zhang, Y.; Ma, R.; Duan, H.; Loiselle, S.A.; Xu, J.; Ma, M. A Novel Algorithm to Estimate Algal Bloom Coverage to Subpixel Resolution in Lake Taihu. *IEEE J. Sel. Top. Appl. Earth Obs. Remote Sens.* **2014**, *7*, 3060–3068. [\[CrossRef\]](#)
27. Kolarik, N.E.; Shrestha, N.; Caughlin, T.; Brandt, J.S. Leveraging high resolution classifications and random forests for hindcasting decades of mesic ecosystem dynamics in the Landsat time series. *Ecol. Indic.* **2024**, *158*, 111445. [\[CrossRef\]](#)
28. Fonseca, A.; Marshall, M.T.; Salama, S. Enhanced Detection of Artisanal Small-Scale Mining with Spectral and Textural Segmentation of Landsat Time Series. *Remote Sens.* **2024**, *16*, 1749. [\[CrossRef\]](#)
29. Palsson, B.; Ulfarsson, M.O.; Sveinsson, J.R. Convolutional Autoencoder for Spectral–Spatial Hyperspectral Unmixing. *IEEE Trans. Geosci. Remote Sens.* **2021**, *59*, 535–549. [\[CrossRef\]](#)
30. Mu, X.; Yang, Y.; Xu, H.; Guo, Y.; Lai, Y.; McVicar, T.R.; Xie, D.; Yan, G. Improvement of NDVI mixture model for fractional vegetation cover estimation with consideration of shaded vegetation and soil components. *Remote Sens. Environ.* **2024**, *314*, 114409. [\[CrossRef\]](#)
31. Mizuochi, H.; Iijima, Y.; Nagano, H.; Kotani, A.; Hiyama, T. Dynamic Mapping of Subarctic Surface Water by Fusion of Microwave and Optical Satellite Data Using Conditional Adversarial Networks. *Remote Sens.* **2021**, *13*, 175. [\[CrossRef\]](#)
32. Ding, Y.; Huang, J.; Xin, L.; Sun, K.; Li, J.; Gao, S. Fusion technology for green tide information in the Yellow Sea detected from multi-source satellite images. In Proceedings of the SPIE 13170, International Conference on Remote Sensing, Surveying, and Mapping (RSSM 2024), Wuhan, China, 12–14 January 2024; SPIE: Bellingham, WA, USA, 2024; Volume 13170. [\[CrossRef\]](#)
33. Fan, J.; Ma, Y.; Liang, T.; Cui, G. Multi-source remote sensing big data mining reveals cross-regional correlation between aquaculture and Enteromorpha disaster outbreaks. *Geo-Spat. Inf. Sci.* **2024**, 1–13. [\[CrossRef\]](#)

34. Chen, Z.; Zhang, L.; Liang, S.; Wang, S.; Zhang, L. Electrical Impedance Tomography for Thorax Image Using Connected Component Labeling and Sparse Group Lasso. *IEEE Trans. Instrum. Meas.* **2024**, *73*, 1–12. [[CrossRef](#)]
35. Evstigneev, N.M.; Ryabkov, O.I.; Gerke, K.M. Stationary Stokes solver for single-phase flow in porous media: A blazingly fast solution based on Algebraic Multigrid Method using GPU. *Adv. Water Resour.* **2023**, *171*, 104340. [[CrossRef](#)]
36. Mehdizadeh, M.; Tavakoli Tafti, K.; Soltani, P. Evaluation of histogram equalization and contrast limited adaptive histogram equalization effect on image quality and fractal dimensions of digital periapical radiographs. *Oral Radiol.* **2023**, *39*, 418–424. [[CrossRef](#)] [[PubMed](#)]
37. Deng, H.; Wen, W.; Zhang, W. Analysis of Road Networks Features of Urban Municipal District Based on Fractal Dimension. *ISPRS Int. J. Geo-Inf.* **2023**, *12*, 188. [[CrossRef](#)]
38. Thore, P.; Lucas, A. Extracting connectivity paths in 3D reservoir property: A pseudo skeletonization approach. *Comput. Geosci.* **2023**, *171*, 105262. [[CrossRef](#)]
39. Ćiprijanović, A.; Lewis, A.; Pedro, K.; Madireddy, S.; Nord, B.; Perdue, G.N.; Wild, S.M. DeepAstroUDA: Semi-supervised universal domain adaptation for cross-survey galaxy morphology classification and anomaly detection. *Mach. Learn. Sci. Technol.* **2023**, *4*, 025013. [[CrossRef](#)]
40. Liu, M.; Pan, J.; Zhu, J.; Chen, Z.; Zhang, B.; Wu, Y. A Sparse SAR Imaging Method for Low-Oversampled Staggered Mode via Compound Regularization. *Remote Sens.* **2024**, *16*, 1459. [[CrossRef](#)]
41. Yang, T.; Han, B.; He, X.; Ye, Z.; Tang, Y.; Lin, J.; Cui, X.; Bi, J. Diagnosis of the accuracy of land cover classification using bootstrap resampling. *Int. J. Remote Sens.* **2024**, *45*, 3897–3912. [[CrossRef](#)]
42. Chen, H.; He, Y.; Zhang, L.; Yang, W.; Liu, Y.; Gao, B.; Zhang, Q.; Lu, J. A Multi-Input Channel U-Net Landslide Detection Method Fusing SAR Multisource Remote Sensing Data. *IEEE J. Sel. Top. Appl. Earth Obs. Remote Sens.* **2024**, *17*, 1215–1232. [[CrossRef](#)]
43. Xiao, Y.; Li, Z.; Zhang, Z. Enhancing Image Perception Quality: Exploring Loss Function Variants in SRCNN. In Proceedings of the 2024 7th International Conference on Computer Information Science and Artificial Intelligence, CISAI '24, Shaoxing, China, 13–15 September 2024; pp. 352–356. [[CrossRef](#)]
44. Wang, X.; Sun, L.; Chehri, A.; Song, Y. A Review of GAN-Based Super-Resolution Reconstruction for Optical Remote Sensing Images. *Remote Sens.* **2023**, *15*, 5062. [[CrossRef](#)]
45. Pang, B.; Zhao, S.; Liu, Y. The Use of a Stable Super-Resolution Generative Adversarial Network (SSRGAN) on Remote Sensing Images. *Remote Sens.* **2023**, *15*, 5064. [[CrossRef](#)]

**Disclaimer/Publisher's Note:** The statements, opinions and data contained in all publications are solely those of the individual author(s) and contributor(s) and not of MDPI and/or the editor(s). MDPI and/or the editor(s) disclaim responsibility for any injury to people or property resulting from any ideas, methods, instructions or products referred to in the content.